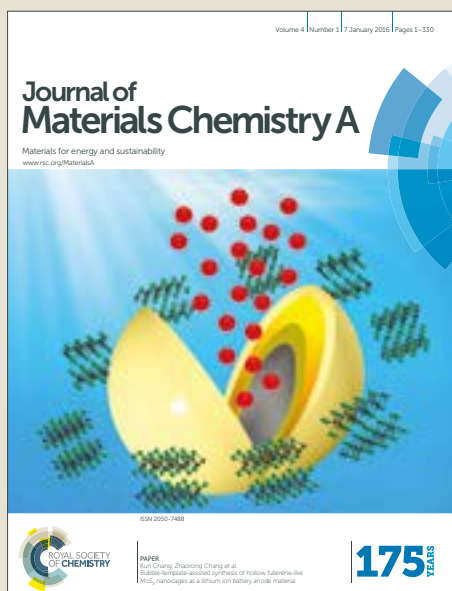


Journal of Materials Chemistry A

Accepted Manuscript



This article can be cited before page numbers have been issued, to do this please use: R. Wang, T. Yan, L. Han, G. Chen, H. Li, J. Zhang, L. Shi and D. Zhang, *J. Mater. Chem. A*, 2018, DOI: 10.1039/C8TA00439K.



This is an Accepted Manuscript, which has been through the Royal Society of Chemistry peer review process and has been accepted for publication.

Accepted Manuscripts are published online shortly after acceptance, before technical editing, formatting and proof reading. Using this free service, authors can make their results available to the community, in citable form, before we publish the edited article. We will replace this Accepted Manuscript with the edited and formatted Advance Article as soon as it is available.

You can find more information about Accepted Manuscripts in the [author guidelines](#).

Please note that technical editing may introduce minor changes to the text and/or graphics, which may alter content. The journal's standard [Terms & Conditions](#) and the ethical guidelines, outlined in our [author and reviewer resource centre](#), still apply. In no event shall the Royal Society of Chemistry be held responsible for any errors or omissions in this Accepted Manuscript or any consequences arising from the use of any information it contains.

Tuning Dimensions and Structures of Nitrogen-doped Carbon Nanomaterials Derived from Sacrificial g-C₃N₄/Metal-Organic Frameworks for Enhanced Electrocatalytic Oxygen Reduction

Ruwen Wang, Tingting Yan, Lupeng Han, Guorong Chen, Hongrui Li, Jianping Zhang, Liyi Shi and Dongsong Zhang*

Received 00th January 20xx,
Accepted 00th January 20xx

DOI: 10.1039/x0xx00000x

www.rsc.org/

Here we demonstrate a facile strategy for tuning the dimensions and structures of nitrogen-doped carbon nanomaterials via regulating the ratio of Co/Zn in zeolitic imidazolate frameworks (ZIFs) arrays in-situ grown on g-C₃N₄ nanosheets followed by a pyrolysis process. One-dimensional nitrogen-doped bamboo-like carbon nanotubes encapsulated Co nanoparticles (Co/N-BCNTs), two-dimensional nitrogen-doped carbon nanosheets (N-CNS) and three-dimensional nitrogen-doped carbon nanotubes frameworks encapsulated Co nanoparticles (Co/N-CNTFs) electrocatalysts are successfully fabricated from Zn/Co-ZIF@g-C₃N₄, ZIF-8@g-C₃N₄ (Co free) and ZIF-67@g-C₃N₄ (Zn free), respectively. The resulting Co/N-BCNTs electrocatalyst exhibits a better oxygen reduction reaction (ORR) activity than the other two catalysts, with a half-wave potential of 0.83 V (*versus* reversible hydrogen electrode) in alkaline solutions, which is superior to the commercial Pt/C catalyst. More importantly, the Co/N-BCNTs shows much higher stability and better methanol-tolerance than those of the Pt/C catalyst in a 0.1M KOH solution. It has been demonstrated that the enhanced catalytic performance of Co/N-BCNTs is attributed to the suitable surface area, well-dispersed N dopants, and Co encapsulated inside of carbon nanotubes. The presented strategy offers new prospects in developing highly active electrocatalysts.

1. Introduction

The increasing desire of energy conversion and storage devices with zero pollution and high efficiency have stimulated extensive efforts toward clean energy technologies including polymer electrolyte membrane fuel cells (PEMFC)¹⁻³, metal-air batteries⁴⁻⁶ and water splitting⁷⁻⁹. The oxygen reduction reaction (ORR) is an extremely crucial process on the cathode which limits the efficiency. The intrinsically sluggish kinetics of ORR calls for efficient electrocatalysts to facilitate the performance^{10,11}. Platinum and its alloys have been employed commercially as catalysts for ORR. Peng and co-workers have reported a series of Pt based catalysts, including octahedral Pt-Ni alloy nanoparticles produced on carbon support¹² and octahedral Pt₂CuNi alloy nanoparticles with uniform element distribution¹³. Yet, the limited platinum reserves, high price and low stability are the primary issues, hindering the large-scale industrialization¹⁴. Thus, considerable efforts have been put into the development of inexpensive and highly efficient substitutes for the noble metal-based ORR electrocatalysts. Carbon nanomaterials are introduced owing to their large

surface area¹⁵, unique geometry, excellent conductivity, and intrinsic flexibility¹⁶. Recently, great progresses have been made in transition metal-nitrogen-carbon electrocatalysts^{17,18} and metal-free heteroatom-doped carbon materials^{19,20}. One-dimensional (1D) carbon nanotubes (CNTs) have extremely high electrical conductivity and remarkable charge transport ability²¹. Nitrogen-doping CNTs have captured much attention over the last several years for ORR application^{22,23}, because nitrogen doping introduces abundant defects in the wall of nanotubes, which provides additional sites for creating positive charges on the adjacent carbon atoms, thus promoting oxygen adsorption and ORR^{24,25}. Bao and co-workers reported an encouraging ORR electrocatalyst with Fe nanoparticles encapsulated within the compartments of peapod like CNTs which exhibited a highly active ORR performance and excellent stability²⁶. Two-dimensional (2D) carbon nanosheets (CNS), especially graphene, are excellent conductors of heat and electricity with light, nearly transparent and robust characteristics²⁷. Recently, Zhang and co-workers successfully synthesized nitrogen-doped carbon nanosheets with a high nitrogen contents (11.6%) which showed excellent ORR activity²⁸. Moreover, three-dimensional (3D) carbon materials are well developed for ORR on account of their distinct nanostructure in all dimensions²⁹⁻³⁴. Metal-organic frameworks (MOFs) as precursors for the preparation of 3D porous carbons exhibit superior exceptionally high surface areas and functionalization properties³⁵⁻³⁷. For example, zeolitic imidazolate frameworks

Research Center of Nano Science and Technology, School of Material Science and Engineering, Shanghai University, Shanghai, 200444, China. E-mail: dszhang@shu.edu.cn

Electronic Supplementary Information (ESI) available: TEM images, AFM images, XRD patterns, LSV curves, XPS information, Comparison of ORR performance for various samples. See DOI: 10.1039/x0xx00000x

(ZIFs), tetrahedrally coordinated transition-metal ions connected by imidazolate linkers³⁸, are excellent precursors for metal/nitrogen-doped carbon (M-N-C) catalysts considering the existence of cobalt and nitrogen species³⁹⁻⁴². Various M-N-C electrocatalysts prepared from ZIFs have shown promising ORR performance⁴³. The nitrogen species in M-N-C not only serve as the heteroatoms but form chemical bonds with metal nanoparticles as well^{44, 45}. Lou, Wang and co-workers developed 3D carbon frameworks of nitrogen-doped CNTs with encapsulated cobalt nanoparticles derived from ZIFs, which exhibited superior electrocatalytic activity and stability for ORR⁴⁶. Therefore, tuning the dimensions and structures of nitrogen-doping carbon nanomaterials is of great significance for enhanced ORR activity.

In this work, we demonstrate a facile strategy to synthesize 1D, 2D and 3D N-doped carbon nanomaterials via regulating the ratio of Co/Zn in zeolitic imidazolate frameworks (ZIFs) arrays in-situ grown on g-C₃N₄ nanosheets followed by a pyrolysis process. Herein, g-C₃N₄ not only serves as a nitrogen source but a template attracting Co²⁺ and Zn²⁺ due to its negative charge on the surface, and thereby Co/Zn-ZIFs could be in-situ grown onto the g-C₃N₄ nanosheets⁴⁷. The resulting 1D nitrogen-doped bamboo-like carbon nanotubes encapsulated Co (Co/N-BCNTs) electrocatalyst exhibits excellent ORR activity, stability and good methanol-tolerance performance, which were attributed to the suitable surface area, well-dispersed N dopants, and Co encapsulated inside of CNTs.

2. Experimental

2.1 Preparation of electrocatalysts

For a typical preparation of g-C₃N₄⁴⁸, urea was heated to 550°C at a rate of 5°C min⁻¹ in a muffle furnace. The peak temperature was maintained at 550°C for 4 h. As a result, g-C₃N₄ nanosheets were obtained after cooling to room temperature.

0.5g g-C₃N₄ was dissolved in 80 ml methanol, and ultrasonic dispersed evenly. Then appointed amount of Zn(NO)₃·6H₂O and 0.4074g Co(NO)₃·6H₂O were added followed by an ultrasonic treatment for 8h. The molar ratio of Zn/Co is 3, 2, 1, 1/2, 1/3, and the total is 2.8mmol. 1.85g 2-methylimidazole was dissolved in 80ml methanol and the former solution was mixed with the latter one and then stirred for 24 h. The obtained products were separated by centrifugation and further repeatedly washed with methanol. After drying in vacuum oven for 12 h at 60 °C, the precursor Zn/Co-ZIF@g-C₃N₄ were obtained.

The as-prepared Zn/Co-ZIF@g-C₃N₄ precursor was heated to 900°C under N₂ with a ramp rate of 3 °C min⁻¹ and then maintained for 1 h. After cooling down to room temperature, the pyrolyzed sample was subjected to acid leaching in HCL for 12 h, then the samples containing metal Co and N-doped Bamboo-like CNTs were obtained, which are designated as Co/N-BCNTs-T (i.e., Co/N-BCNTs-800), where T represents the pyrolysis temperature.

The synthetic procedure of 2D N-CNS electrocatalysts was similar to that of Co/N-BCNTs electrocatalysts, but the metal source was replaced by 0.84g Zn(NO)₃·6H₂O. The synthetic procedure of 3D Co/N-CNTFs electrocatalysts was also similar to that of Co/N-BCNTs electrocatalysts, but the metal source was replaced by 0.4074g Co(NO)₃·6H₂O and the amount of 2-methylimidazole decreased to 0.925g.

2.2 Instrumental

Structural Characterization: Scanning electron microscopy (SEM) analysis were carried out on a JSM-7001F SEM unit. Transmission electron microscope (TEM) were conducted on a JEOL JEM-200CX. High resolution transmission electron microscopy (HRTEM) images were obtained using a JEOL JEM-2010F instrument. Raman spectra were acquired using a JY H800UV instrument. The XRD patterns were recorded by a Rigaku D/MAX-RB X-ray diffractometer. Nitrogen adsorption-desorption isotherms were measured with an ASAP 2020 (Micromeritics) at -196°C. Raman-mapping images were conducted on a Confocal Raman microscope in Via. The adsorption data were used to calculate the specific surface areas by the Brunauer-Emmett-Teller (BET) method. Pore size distribution curves were obtained from the desorption branches of the isotherms by the Barrett-Joyner-Halenda (BJH) method. X-ray photoelectron spectroscopic (XPS) measurements were conducted on a Perkin-Elmer PHI 5000C ESCA using a twin anode Mg Ka (1253.6 eV) radiation. Atomic Force Microscope (AFM) analysis was carried out on a Park NX10.

2.3 Electrochemical Characterization

The working electrode was prepared as follows: The catalyst ink was made of as-synthesized catalyst (5 mg), 5 wt.% Nafion solution (0.2 mL), ethanol (0.2 mL) and deionized water (0.6 mL) under sonication for 1h. Then 8 μL of the resulting suspension was dropped onto a pre-polished glassy carbon electrode (D = 5 mm) and dried at room temperature. For comparison, a commercially 20 wt.% Pt/C electrocatalyst (JM) was used. The electrode preparation was identical to that used for the Co/N-BCNTs. The electrochemical measurements were conducted on a CHI 760E with a three-electrode system. A glassy carbon rotating disk electrode coated with electrocatalyst was used as the working electrode, and an Ag/AgCl electrode and a Pt foil were used as the reference and counter electrodes, respectively. The oxygen reduction reaction was carried out in an O₂ saturated 0.1 M KOH aqueous solution (100 mL). The durability test for methanol was carried out in an O₂ saturated 0.1 M KOH aqueous solution, and 5 mL methanol was added around 400 s. In addition, the current was collected at -0.25 V (*versus* Ag/AgCl) and the rotation speed is 1600 rpm.

2.4 Calculation of electron transfer number (n)

The Koutecky-Levich (K-L) plots (J_{-1} vs $\omega^{-1/2}$) were collected at various electrode potentials (0.2 V, 0.3 V, 0.4 V, 0.5 V and 0.6 V respectively). The electron transfer number was calculated from the slopes of Koutecky-Levich equation⁴⁹ (S1):

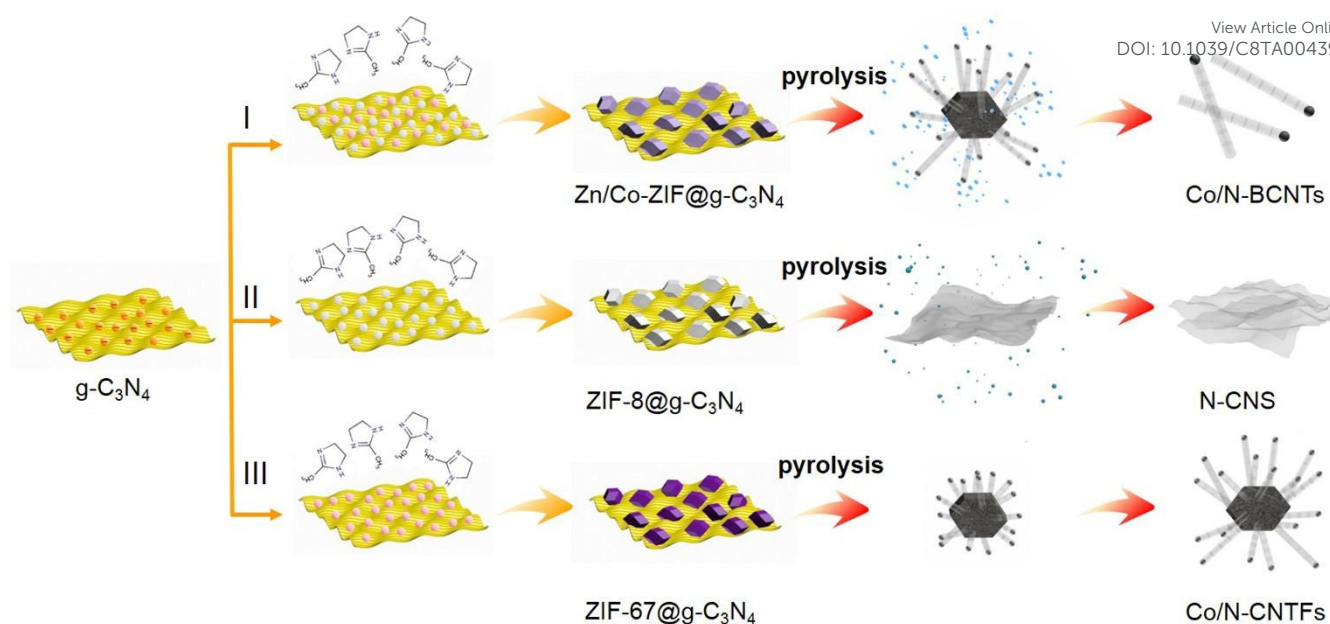


Figure 1. Schematic illustration for the preparation of nitrogen-doped carbon nanomaterials.

$$\frac{1}{J} = \frac{1}{J_k} + \frac{1}{B\omega^{0.5}} \quad (\text{S1})$$

Where J_k and ω refers to the kinetic current and the electrode rotating rate, respectively. B is determined from the slope of K - L plots based on Levich equation⁵⁰ (S2):

$$B = 0.2nFv \frac{1}{6} C_{\text{O}_2} (D_{\text{O}_2})^{\frac{2}{3}} \quad (\text{S2})$$

where n is the electron transfer number per oxygen molecule, F refers to the Faraday constant ($F = 96485 \text{ C mol}^{-1}$), D_{O_2} is the diffusion coefficient of O_2 ($1.9 \times 10^{-5} \text{ cm}^2 \text{ s}^{-1}$ in 0.1 M KOH), v is the kinetic viscosity of the electrolyte ($v = 0.01 \text{ cm}^2 \text{ s}^{-1}$ in 0.1 M KOH), and C_{O_2} is the concentration of O_2 ($1.2 \times 10^{-3} \text{ mol L}^{-1}$). When the rotating speed is in rpm, the constant 0.2 is adopted.

3. Results and discussion

3.1 Morphology and structure of the electrocatalysts

A schematic diagram illustrating the catalyst synthesis is shown in Scheme 1 and the route I, II and III correspond to 1D, 2D and 3D nitrogen-doped materials, respectively. First, $g\text{-C}_3\text{N}_4$ was synthesized by thermal decomposition-polymerization of urea. The resulting product exhibit a sheet-like structure with various pores (Figure S1a). We used $g\text{-C}_3\text{N}_4$ as both the nitrogen source and templates adsorbing Co^{2+} and Zn^{2+} on the surface. Subsequently, Zn/Co-ZIF (Figure 1, Route I), ZIF-8 (Figure 1, Route II) and ZIF-67 (Figure 1, Route III) were in-situ grown on both sides of $g\text{-C}_3\text{N}_4$ nanosheets, and the product was designated as Zn/Co-ZIF@ $g\text{-C}_3\text{N}_4$ (Route I,), ZIF-8@ $g\text{-C}_3\text{N}_4$ (Co free, Route II) and ZIF-67@ $g\text{-C}_3\text{N}_4$ (Zn free, Route III) respectively. Typically, it has been demonstrated that Zn/Co-ZIF is in-situ grown the $g\text{-C}_3\text{N}_4$ nanosheets (Figure S1b).

Interestingly, nitrogen-doped carbon nanomaterials with disparate dimensions are achieved after a thermal treatment. In Route I, 1D nitrogen-doped Figure 1a) are obtained from Zn/Co-ZIF@ $g\text{-C}_3\text{N}_4$. It is observed that the $g\text{-C}_3\text{N}_4$ as templates decomposes completely and Zn/Co-ZIF as precursors undergoes pyrolysis to afford bamboo-like nanotubes with a diameter of 25-110 nm (Figure 2a-e). Besides, Co nanoparticles are encapsulated inside of the CNTs with a diameter of 20-100 nm. HRTEM images show the lattice fringes of these multi-walled bamboo-like CNTs. The inter-planar distance is 0.36 nm that corresponds to the C (002) plane (Figure 2f). The elemental distribution was investigated using EDS mapping as shown in Figure 2g-k. Along the bamboo-like CNTs, it is obvious that Co (green) is concentrated in the inside of CNTs, while C (purple), N (blue) and O (red) were distributed on the whole CNT surface, verifying the formation of the Co/N-BCNTs and the carbon-encased nanoparticles. The structure feature observed is in agreement with the XRD results (Figure 4a). A typical strong peak at $\sim 26^\circ$ is observed, which is attributed to the (002) facets of graphite carbon, and the peaks located at 44.3° , 51.5° , and 75.7° correspond to metallic Co (111), Co (200), and Co (220), respectively⁵¹. In Route II, we successfully synthesized 2D N-doped carbon nanosheets (N-CNS) derived from ZIF-8@ $g\text{-C}_3\text{N}_4$ (Co free). As shown in Figure 3a and 3b, the sheets with large pores are nearly transparent. AFM images show that the average thickness of nanosheet is around 4 nm, which contains about 12 atomic layers (Figure S2). XRD patterns reveal a graphite-related peak at 26° (Figure 4a). Meanwhile, we obtained nitrogen-doped carbon nanotubes frameworks encapsulated Co nanoparticles (Co/N-CNTFs) originated from ZIF-67@ $g\text{-C}_3\text{N}_4$ (Zn free). As shown in Figure 3c and 3d, the polyhedral shape of ZIF-67 was partially retained, while many bamboo-like CNTs with packaged Co nanoparticles can be observed on the surface. The XRD pattern (Figure 4a) shows that the peak located at about 26° corresponding to the

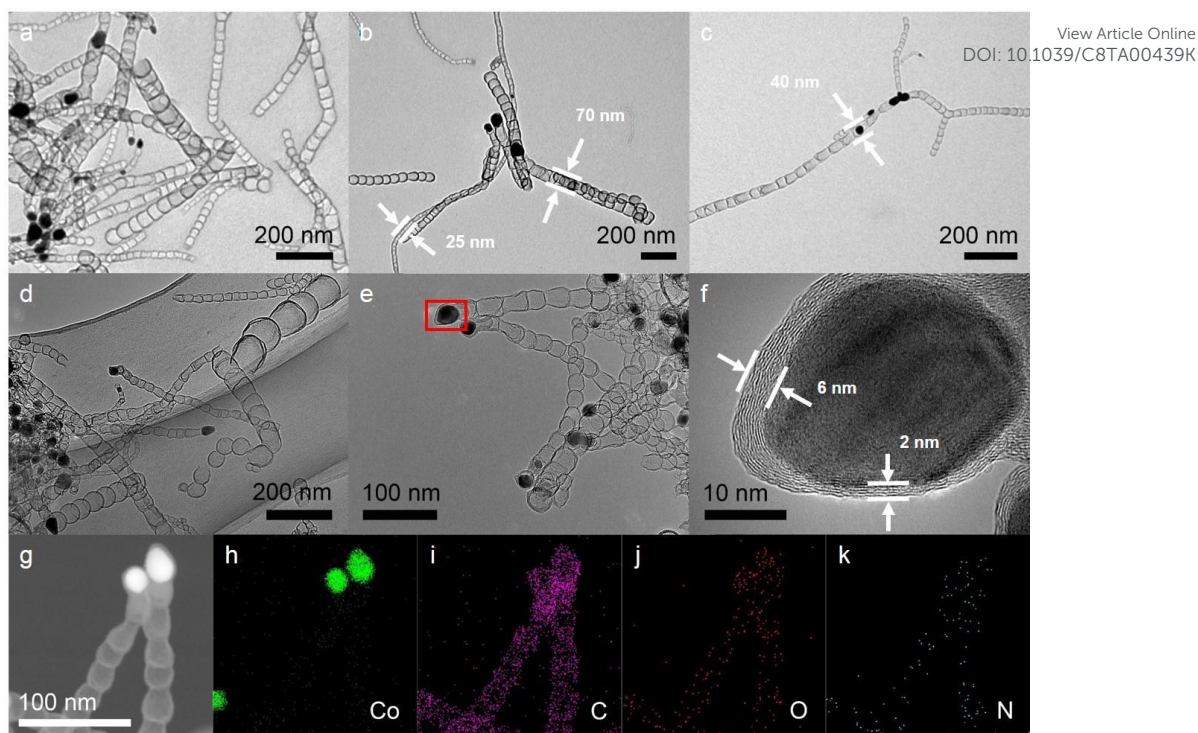


Figure 2. (a-c) TEM images, (d-f) HRTEM images, (g-k) HAADF/STEM images and the corresponding EDS elemental mapping (Co, C, O, and N) of Co/N-BCNTs.

C (002) plane, and the peaks at 44.3° , 51.5° , and 75.7° are attributed to metallic Co (111), Co (200), and Co (220), respectively.

A Raman spectrum was used to analyse the graphitic level of various carbon nanostructures. Specifically, peaks at 1345, 1580, and 2684 cm^{-1} (Figure 4b) correspond to the well-defined D, G, and 2D bands³⁶, respectively. It has been demonstrated that the G band can be utilized to analyse the degree of graphitization, while the D band is associated with partial disorders or defects of the graphitic domains⁵². For Co/N-BCNTs and Co/N-CNTFs, the G bands exhibit stronger than D bands, along with a sharp 2D band suggesting a

relatively high degree of graphitization and the existence of few-layer graphene-like structures. The I_D/I_G value is generally used to evaluate the amount of defects or graphitization degree of carbon materials⁵³. The Raman-mapping was used to provide the distribution of I_G (Figure 5a, 5c and 5e) and I_D/I_G (Figure 5b, 5d and 5f). The I_D/I_G value of Co/N-BCNTs is 1.18-1.46 (Figure 5b), between that of N-CNS (Figure 5d) and Co/N-CNTFs (Figure 5f), which probably results in suitable defects and degree of graphitization. What's more, the N-CNS exhibits a relatively homogeneous and high I_D/I_G value within 1.55-1.73 (Figure 5d), probably attributed to more structural defects derived from the insertion of nitrogen atoms into the sp^2 -carbon hexagonal network. In contrast, the Co/N-CNTFs show a smaller I_D/I_G value ranged from 0.97 to 1.26 (Figure 5f), indicating the relatively high graphitization level which will surely improve electrical conductivity, thus promoting the ORR activity⁵⁴.

The N_2 adsorption and desorption isotherms are used to analyse the specific surface area and pore size distribution (Figure 4c and 4d). All samples show the IV-type curves with an obvious hysteresis confirming the presence of mesoporous, which is probably attributed to the decomposition of $g\text{-C}_3\text{N}_4$, evaporation of Zn during the heat treatment and the inherent porous structure of ZIFs⁵⁵. For N-GNS, the rapid N_2 uptake ($P/P_0 > 0.9$) is originated from the existence of secondary and large pores. The pore size distribution profiles indicate the mesoporous are mainly in the range of 3-5 nm (Figure 4d). Moreover, the sample of N-CNS exhibits the maximum specific surface area ($477\text{ m}^2\text{g}^{-1}$), larger than that of Co/N-BCNTs ($359\text{ m}^2\text{g}^{-1}$) and Co/N-CNTFs ($351\text{ m}^2\text{g}^{-1}$), probably owing to the evaporation of Zn and completely decomposition of $g\text{-C}_3\text{N}_4$.

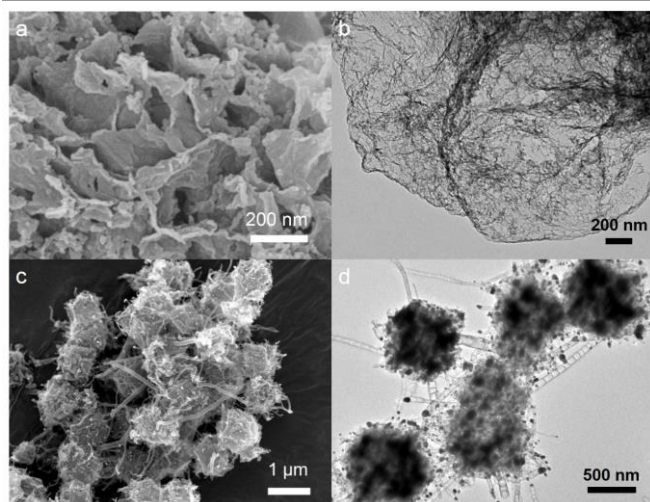


Figure 3. (a) SEM and (b) TEM images of N-CNS; (c) SEM and (d) TEM images of Co/N-CNTFs.

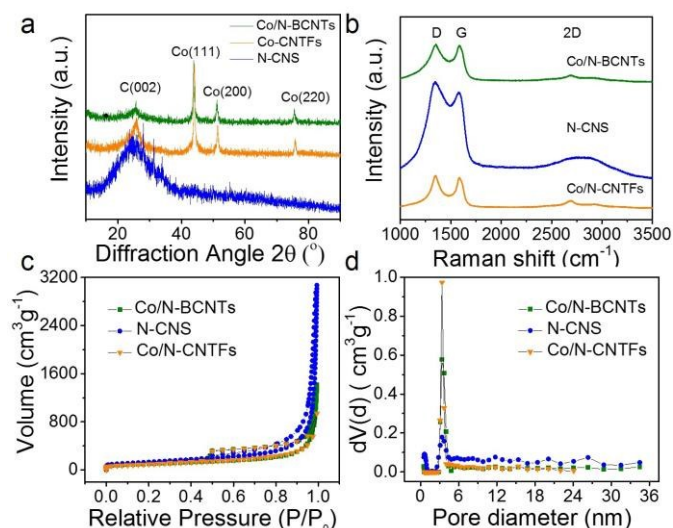


Figure 4. (a) XRD patterns, (b) Raman spectra, (c) N₂ adsorption-desorption isotherms, and (d) BJH pore size distribution profiles of various samples.

The XPS was used to survey the surface species of all materials. Elements of C, N, O, and Co, with no signals of Zn, can be observed on all samples. In the high-resolution C 1s spectrum (Figure 6a), the main peaks centred at about 284.6 eV are attributed to the graphitic sp² carbon, whereas the additional component centred at 285.6 eV is assigned to C-N and/or C=N, conforming the insertion of nitrogen atoms into the basal plane of graphitic carbon. The low intensity of broad band (287.9 eV) typically corresponded to O-C=O. Furthermore, the chemical states of the nitrogen dopants are presented on the high-resolution N 1s spectra. Three different types of nitrogen configurations centred at 398.3 eV, 400.1 eV, and 401.2 eV are found, assigned to pyridinic N, pyrrolic N, and

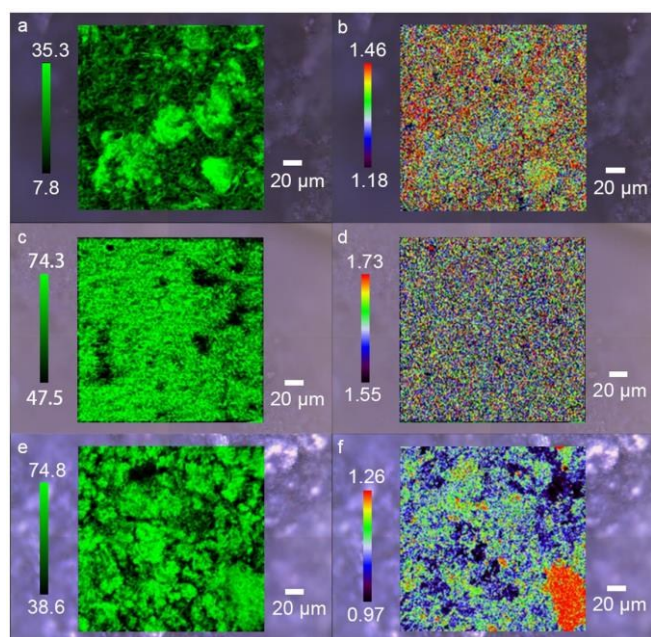


Figure 5. Raman mapping images of (a) I_G and (b) I_D/I_G for Co/N-BCNTs; Raman mapping images of (c) I_G and (d) I_D/I_G for N-CNS; Raman mapping images of (e) I_G and (f) I_D/I_G for Co/N-CNTFs.

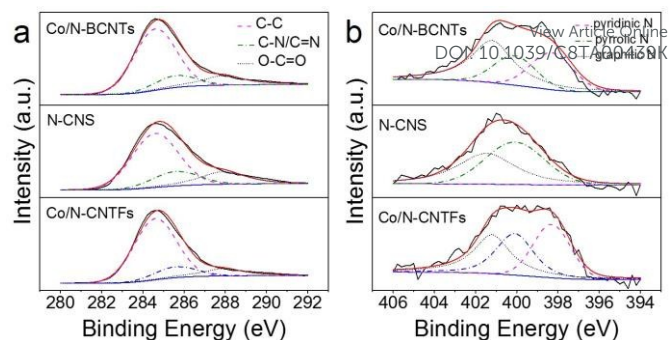


Figure 6. (a) C 1s and (b) N 1s XPS spectra of the catalysts.

graphitic N, respectively (Figure 6b)²⁵. The pyrolysis resulted in a significant difference in the nitrogen-carbon bonding states of the samples. The nitrogen content of Co/N-BCNTs reaches 8.04% with a pyridinic N content of 2.49%, which is superior to that of the other two samples (Table S1 and S2). For N-CNS, no signals of pyridinic N are found. What's more, the nitrogen loss of Co/N-CNTFs is very serious, which is probably due to the volatility of nitrogen at high temperature. It is worth noting that the pyridinic N content of Co/N-BCNTs-T decreases from 2.82% to 2.07% as the annealing temperature increases from 800 °C to 1000 °C (Table S2, Figure S3). Recently, it has been confirmed that a high pyridinic N content can elevate current density, spin density, and the density of π states of the C atoms³¹. Therefore, a high proportion of doped pyridinic N is very desirable for highly active ORR catalysts.

Based on the above obtained results, the formation mechanism of 1D, 2D and 3D carbon materials is proposed. Firstly, it has been demonstrated that g-C₃N₄ not only serves as a nitrogen source but a template attracting Co²⁺ and Zn²⁺ to construct Co/Zn-ZIFs on the surface. What's more, g-C₃N₄ decomposed completely during the heating treatment, not only generating pores but promoting the formation of new structures, because ZIFs are difficult to crack at high temperature in the absence of g-C₃N₄. The morphologies of Zn-Co-ZIF, ZIF-8 and ZIF-67 after the pyrolysis were demonstrated in Figure S4. It is obvious that no bamboo-like CNTs were generated (Figure S4a). ZIF-8-900 and ZIF-67-900 retained the polyhedron structure of ZIF-8 and ZIF-67, respectively (Figure S4b and S4c). It has been proved that g-C₃N₄ is beneficial to the generation of new structures. Meanwhile, during the heating treatment, the synergistic effect of g-C₃N₄ and Co (XRD results, Figure 4a) facilitated the growth of CNTs (Route I and III in Figure 1). On the contrary, no CNTs are generated from ZIF-8@ g-C₃N₄ (Co free, Route II). Zn in ZIFs is easily evaporated at high temperature⁵⁶. The synergistic effect of g-C₃N₄ and Zn not only led to the production of mesoporous but also boosted the completely crack of polyhedron ZIFs (Route I and II). In contrast, the samples derived from ZIF-67@ g-C₃N₄ (Zn free, Route III) partially retained the polyhedron structure of ZIFs. Furthermore, the synergistic effect of g-C₃N₄, Zn and Co facilitated the formation of bamboo-like CNTs encapsulated Co nanoparticles and the completely crack of ZIFs (Route I). Additionally, we also found that bamboo-like CNTs encapsulated Co nanoparticle structure could also be prepared

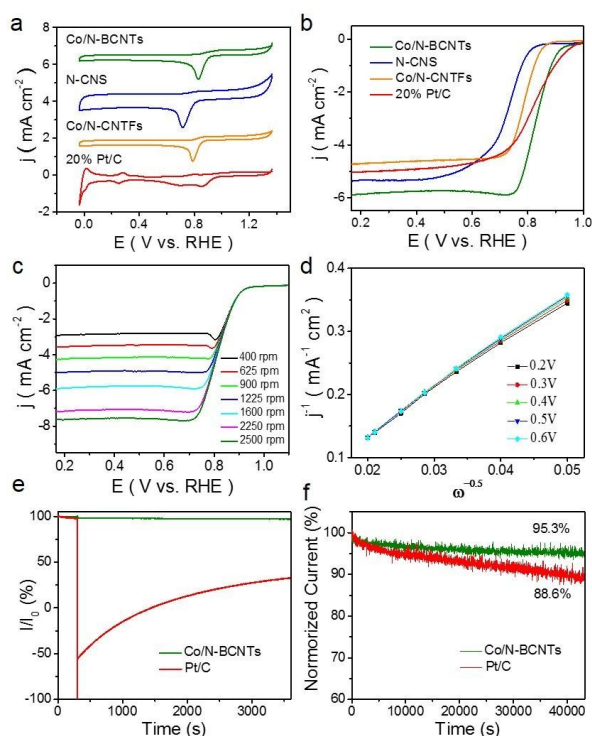


Figure 7. (a) CV curves of all catalysts in O_2 -saturated 0.1M KOH solution. (b) LSV curves in an O_2 -saturated 0.1 M KOH solution at a sweep rate of 10 mV s^{-1} and electrode rotation speed of 1600 rpm. (c) LSV curves of Co/N-BCNTs at various rotation rates. (d) Corresponding Koutecky–Levich plots of Co/N-BCNTs. (e) Current–time (I–t) curves of Co/N-BCNTs and Pt/C in O_2 -saturated 0.1 M KOH solution without and with 5 mL MeOH solution at 0.7 V versus RHE and 1600 rpm. (f) I–t curves of Co/N-BCNTs and Pt/C in O_2 -saturated 0.1 M KOH solution at 0.7 V versus RHE and 400 rpm.

when tuning the ratio of Zn/Co from 3, 2, 1/2, to 1/3 (Figure S5 and S6).

3.2 ORR performance

The desirable structural information reveals the great potential for electrocatalysis. The ORR performance of all as-prepared catalysts is first analyzed by cyclic voltammetry (CV) in alkali media (0.1 M KOH) at room temperature. As shown in Figure 7a, well-defined cathodic peaks are clearly observed at about 0.8 V versus RHE for Co/N-BCNTs, N-CNS and Co/N-CNTFs in an O_2 -saturated 0.1 M KOH solution, confirming the catalytic activities for ORR. Linear Sweep Voltammetry (LSV) measurements are further performed to investigate the ORR activities of the as-prepared catalysts. The LSV data indicate that N-CNS and Co/N-CNTFs show relatively limited activities (half-wave potentials of ~ 0.73 and ~ 0.79 V, respectively) and a small limiting current density as well (Figure 7b), which are still better than Zn-ZIF-900 and Co-ZIF-900, respectively (Figure S7). In contrast, the Co/N-BCNTs shows a higher ORR activity with a half-wave potential of ~ 0.83 V versus RHE as well as a larger limiting current density of 6 mA cm^{-2} , which is even superior to that of Pt/C (half-wave potential of ~ 0.82 V versus RHE and limiting current density of 5.37 mA cm^{-2}). Additionally, the higher limiting current density of Co/N-BCNTs indicates a highly efficient mass transport pathway. Compared with many previously reported Co-N-C electrocatalysts (Table S3)

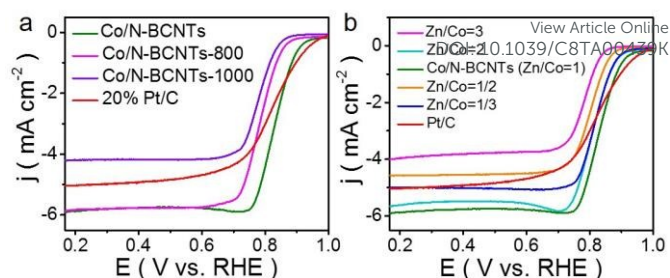


Figure 8. Linear sweep voltammetry (LSV) curves of (a) Co/N-BCNTs-T (b) Zn/Co=X/Y derived Co/N-BCNTs in O_2 -saturated 0.1 M KOH solution at a sweep rate of 10 mV s^{-1} and an electrode rotation speed of 1600 rpm.

measured in 0.1M KOH, the Co/N-BCNTs electrocatalysts exhibit a more positive half-wave potential, indicating a superior ORR performance.

The ORR polarization curves of the electrocatalysts are collected at different rotating speeds (Figure 7c, S8a and S8c) to further explore the electron transfer numbers (n). The linearity of Koutecky–Levich (K–L) plots for Co/N-BCNTs shows a good parallel linearity, indicating a first-order reaction kinetics with respect to the concentration of dissolved O_2 ⁵⁷ (Figure 7d). The value of n at 0.5 V derived from K–L plot is 3.75, close to the theoretical value of Pt/C (4.0), confirming a near $4e^-$ transfer pathway of ORR. Whereas n for N-CNS at the same potential is only 3.62, suggesting the existence of the $2e^-$ pathway (Figure S8b). Generally, the ORR can follow an efficient one-step $4e^-$ process to produce H_2O directly and a two-step $2e^-$ process with the formation of H_2O_2 as well. Furthermore, H_2O_2 as intermediate may poison the electrocatalyst by the oxidation of N ligands⁴⁶.

The carbonization temperature significantly influences the ORR performance of the Co/N-BCNTs-T. With the temperature increasing from 800°C to 1000°C , the pyridinic N content decreases, but the graphitization degree is improved. It has been demonstrated that, the pyridinic N content provides highly active sites for the ORR. Besides, higher graphitization degree promotes the rate of electron transfer. Hence, there is a most suitable temperature between 800°C and 1000°C . Figure 8 (a) shows the ORR activities of Co/N-BCNTs-T between 800°C and 1000°C . Comparatively, the sample Co/N-BCNTs exhibits the best ORR activity at 900°C , attributed to its relatively higher pyridinic N content and graphitization degree. In addition, at a fixed temperature of 900°C , the ORR activity shows a sharply decline with the ratio of Zn/Co changed from 1, 2, 1/3, 1/2 to 3 (Figure 8b), which could be due to the aggregation of cobalt nanoparticles (Figure S5a and S5b) and the thicker CNTs walls (Figure S5c and S5d).

Current versus time (i-t) chronoamperometric measurements were carried out to test the methanol-tolerance of Co/N-BCNTs catalysts, which is a key parameter for the practical applications. As shown in Figure 7e, when adding 5ml methanol into the O_2 -saturated 0.1 M KOH solution, the current for Co/N-BCNT-900 is slightly change. On the contrary, there is a conspicuous decrease in current density for commercial Pt/C catalyst, suggesting that Co/N-BCNTs shows

high selectivity for ORR with a strong tolerance to crossover effects.

Furthermore, the long-term stability of Co/N-BCNTs was also confirmed by CA measurements. Figure 7f shows only 5 % current reduction for the Co/N-BCNTs catalyst after a 12 h CA test, whereas more than 11 % of its initial activity was lost for the Pt/C catalyst under the same condition (0.7 V with O₂ continuous flow in 0.1 M KOH), further proving a superb durability of the Co/N-BCNTs catalyst toward ORR. It may be attributed to that encapsulated Co nanoparticles are physically isolated from the harsh environment and thus avoiding leaching.

It has been demonstrated that encapsulated the metallic nanoparticles in CNTs could improve electrocatalytic activity because of the electronic interaction between CNTs and metal nanoparticles^{26, 46}. What's more, well-dispersed N dopants, appropriate degree of graphitization and suitable surface area of Co/N-BCNTs are all beneficial to ORR activities, which is agreement with the ORR test of Co/N-BCNTs. It has been confirmed that Co/N-BCNTs exhibited the best ORR performance in terms of onset potential, half-wave potential and limiting current density.

4. Conclusions

In conclusion, we have demonstrated a facile and effective method to synthesize nitrogen-doped carbon nanomaterials with tunable dimensions and structures via a directed growth of ZIFs arrays on g-C₃N₄ followed by a heat treatment. By tuning the content of Co and Zn on the g-C₃N₄ layer, 1D nitrogen-doped bamboo-like carbon nanotubes encapsulated Co nanoparticles, 2D nitrogen-doped carbon nanosheets and 3D nitrogen-doped carbon nanotubes frameworks encapsulated Co nanoparticles electrocatalysts have been successfully obtained. All of them have hierarchical nanostructures and uniform heteroatom doping. The newly designed Co/N-BCNTs catalyst exhibits a high ORR activity in alkaline medium. Meanwhile, the excellent durability and extraordinary methanol tolerance are even better than commercial Pt/C catalyst. More importantly, this progress provides a new path to regulate the dimensions and structures of N-doped carbon nanomaterials and may be extended to prepare other carbon nanomaterials/metal nanoparticles hybrids toward electrocatalytic reactions.

Conflicts of interest

There are no conflicts to declare.

Acknowledgements

This work was financially supported by the National Natural Science Foundation of China (21722704), and the Science and Technology Commission of Shanghai Municipality (16DZ1204300, 15DZ2281400 and 16JC1401700).

Notes and references

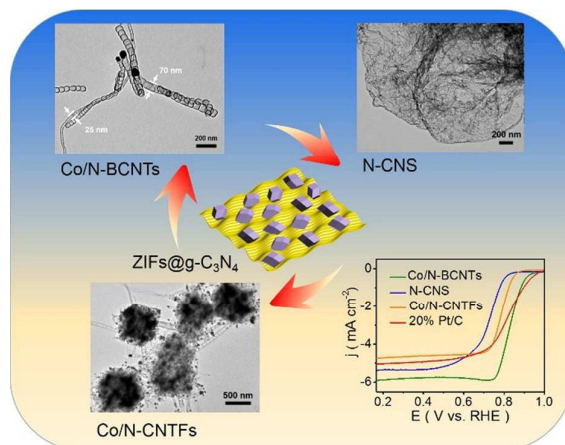
- 1 E. Proietti, F. Jaouen, M. Lefevre, N. Larouche, J. Tian, J. Herranz, J.P. Dodelet, *Nat. Commun.*, 2011, **2**, 416.
- 2 T. Sun, B. Tian, J. Lu, C. Su, *J. Mater. Chem. A*, 2017, **5**, 18933
- 3 D. He, H. Tang, Z. Kou, M. Pan, X. Sun, J. Zhang, S. Mu, *Adv. Mater.*, 2017, **29**, 1601741.
- 4 M. Yu, Z. Wang, C. Hou, Z. Wang, C. Liang, C. Zhao, Y. Tong, X. Lu, S. Yang, *Adv. Mater.*, 2017, **29**, 1602868.
- 5 M. Zeng, Y. Liu, F. Zhao, K. Nie, N. Han, X. Wang, W. Huang, X. Song, J. Zhong, Y. Li, *Adv. Funct. Mater.*, 2016, **26**, 4397-4404.
- 6 Z. Peng, S. A. Freunberger, Y. Chen, P. G. Bruce, *Science*, 2012, **337**, 563-566.
- 7 Z. Wu, X. Wang, J. Huang, F. Gao, *J. Mater. Chem. A*, 2018, **6**, 167
- 8 M. Blasco-Ahicart, J. Soriano-López, J.J. Carbó, J.M. Poblet, J.R. Galan-Mascaros, *Nat. chem.*, 2017.
- 9 L. Yu, H. Zhou, J. Sun, F. Qin, D. Luo, L. Xie, F. Yu, J. Bao, Y. Li, Y. Yu, S. Chen, Z. Ren, *Nano Energy*, 2017, **41**, 327-336.
- 10 M.K. Debe, *Nature*, 2012, **486**, 43-51.
- 11 M. Sun, D. Davenport, H. Liu, J. Qu, M. Elimelech, J. Li, *J. Mater. Chem. A*.
- 12 C. Zhang, S. Y. Hwang, A. Trout, Z. Peng, *J. Am. Chem. Soc.*, 2014, **136**, 7805-7808.
- 13 C. Zhang, W. Sandorf, Z. Peng, *ACS Catal.*, 2015, **5**, 2296-2300.
- 14 J.A. Varnell, E.C. Tse, C.E. Schulz, T.T. Fister, R.T. Haasch, J. Timoshenko, A.I. Frenkel, A.A. Gewirth, *Nat. Commun.*, 2016, **7**, 12582.
- 15 M. Hu, J. Reboul, S. Furukawa, N.L. Torad, Q. Ji, P. Srinivasu, K. Ariga, S. Kitagawa, Y. Yamauchi, *J. Am. Chem. Soc.*, 2012, **134**, 2864-2867.
- 16 J. Ni, Y. Li, *Adv. Energy. Mater.*, 2016, **6**, 1600278.
- 17 W.J. Jiang, L. Gu, L. Li, Y. Zhang, X. Zhang, L.J. Zhang, J.Q. Wang, J.S. Hu, Z. Wei, L.J. Wan, *J. Am. Chem. Soc.*, 2016, **138**, 3570-3578.
- 18 Y. Han, Y. Wang, W. Chen, R. Xu, L. Zheng, J. Zhang, J. Luo, R. Shen, Y. Zhu, W. Cheong, C. Chen, Q. Peng, D. Wang, Y. Li, *J. Am. Chem. Soc.*, 2017, **139**, 17269-17272.
- 19 J. Zhang, L. Qu, G. Shi, J. Liu, J. Chen, L. Dai, *Angew. Chem.*, 2016, **55**, 2230-2234.
- 20 Y. Yao, Z. Chen, A. Zhang, J. Zhu, X. Wei, J. Guo, W. D. Wu, X. D. Chen and Z. Wu, *J. Mater. Chem. A*, 2017, **5**, 25237
- 21 K. Hata, D. N. Futaba, K. Mizuno, T. Namai, M. Yumura, S. Iijima, *Science*, 2004, **306**, 1362-1364.
- 22 J. Liang, R.F. Zhou, X.M. Chen, Y.H. Tang, S.Z. Qiao, *Adv. Mater.*, 2014, **26**, 6074-6079.
- 23 C. Zhu, S. Fu, J. Song, Q. Shi, D. Su, M.H. Engelhard, X. Li, D. Xiao, D. Li, L. Estevez, D. Du, Y. Lin, *Small*, 2017, 1603407.
- 24 Y. Liu, Y. Shen, L. Sun, J. Li, C. Liu, W. Ren, F. Li, L. Gao, J. Chen, F. Liu, Y. Sun, N. Tang, H. Cheng, Y. Du, *Nat. Commun.*, 2016, **7**, 10921.
- 25 X. Cui, S. Yang, X. Yan, J. Leng, S. Shuang, P.M. Ajayan, Z. Zhang, *Adv. Funct. Mater.*, 2016, **26**, 5708-5717.
- 26 D. Deng, L. Yu, X. Chen, G. Wang, L. Jin, X. Pan, J. Deng, G. Sun, X. Bao, *Angew. Chem.*, 2013, **52**, 371-375.
- 27 A. K. Geim, *Science*, 2009, **324**, 1530-1534.
- 28 H. Yu, L. Shang, T. Bian, R. Shi, G.I. Waterhouse, Y. Zhao, C. Zhou, L.Z. Wu, C.H. Tung, T. Zhang, *Adv. Mater.*, 2016, **28**, 5080-5086.
- 29 C. Zhang, B. Wang, X. Shen, J. Liu, X. Kong, S. S. C. Chuang, D. Yang, A. Dong, Z. Peng, *Nano Energy*, 2016, **30**, 503-510.
- 30 Z. Li, M. Shao, Q. Yang, Y. Tang, M. Wei, D.G. Evans, X. Duan, *Nano Energy*, 2017, **37**, 98-107
- 31 T.Y. Ma, S. Dai, M. Jaroniec, S.Z. Qiao, *Angew. Chem.*, 2014, **53**, 7281-7285.

View Article Online
DOI: 10.1039/C8TA00439K

- 32 J. Wei, Y. Liang, Y. Hu, B. Kong, J. Zhang, Q. Gu, Y. Tong, X. Wang, S.P. Jiang, H. Wang, *Angew. Chem.*, 2016, **55**, 12470-12474.
- 33 Z. Wang, T. Yan, L. Shi, D. Zhang, *ACS Appl. Mater. Interfaces*, 2017, **9**, 15068-15078.
- 34 H. Duan, T. Yan, G. Chen, J. Zhang, L. Shi, D. Zhang, *Chem. Commun.*, 2017, **53**, 7465-7468.
- 35 W. Gu, L. Hu, J. Li, E. Wang, *ACS Appl. Mater. Interfaces*, 2016, **8**, 35281-35288.
- 36 S. Liu, Z. Wang, S. Zhou, F. Yu, M. Yu, C.Y. Chiang, W. Zhou, J. Zhao, J. Qiu, *Adv. Mater.*, 2017, 1700874.
- 37 S. Liu, Z. Wang, S. Zhou, F. Yu, M. Yu, C.Y. Chiang, W. Zhou, J. Zhao, J. Qiu, *Adv. Mater.*, 2017, 1700874.
- 38 C. Zhang, Y. Wang, B. An, R. Huang, C. Wang, Z. Zhou, W. Lin, *Adv. Mater.*, 2017, **29**.
- 39 L. Shang, H. Yu, X. Huang, T. Bian, R. Shi, Y. Zhao, G. I. N. Waterhouse, L. Z. Wu, C. H. Tung, T. Zhang, *Adv. Mater.*, 2016, **28**, 1668-1674.
- 40 L. Huang, X. Zhang, Y. Han, Q. Wang, Y. Fang, S. Dong, *J. Mater. Chem. A*, 2017, **5**, 18610.
- 41 Z. Li, M. Shao, L. Zhou, R. Zhang, C. Zhang, M. Wei, D.G. Evans, X. Duan, *Adv. Mater.*, 2016, **28**, 2337-2344.
- 42 S. Wang, J. Qin, T. Meng, M. Cao, *Nano Energy*, 2017, **39**, 626-638.
- 43 H.X. Zhong, J. Wang, Y.W. Zhang, W.L. Xu, W. Xing, D. Xu, Y.F. Zhang, X.B. Zhang, *Angew. Chem.*, 2014, **53**, 14235-14239.
- 44 X. Wang, H. Zhang, H. Lin, S. Gupta, C. Wang, Z. Tao, H. Fu, T. Wang, J. Zheng, G. Wu, X. Li, *Nano Energy*, 2016, **25**, 110-119.
- 45 L. Zhou, C. Yang, J. Wen, P. Fu, Y. Zhang, J. Sun, H. Wang, Y. Yuan, *J. Mater. Chem. A*, 2017, **5**, 19343.
- 46 B.Y. Xia, Y. Yan, N. Li, H.B. Wu, X.W. Lou, X. Wang, *Nat. Energy*, 2016, **1**, 15006.
- 47 J. Xu, F. Xu, M. Qian, F. Xu, Z. Hong, F. Huang, Conductive Carbon Nitride for Excellent Energy Storage, *Adv. Mater.*, 2017, **29**, 1701674.
- 48 D.A. Giannakoudakis, N.A. Travlou, J. Secor, T.J. Bandosz, *Small*, 2017, **13**, 1601758.
- 49 S. Wang, D. Yu, L. Dai, *J. Am. Chem. Soc.*, 2011, **133**, 5182-5185.
- 50 Z.K. Yang, L. Lin, A.W. Xu, *Small*, 2016, **12**, 5710-5719.
- 51 P. Yin, T. Yao, Y. Wu, L. Zheng, Y. Lin, W. Liu, H. Ju, J. Zhu, X. Hong, Z. Deng, G. Zhou, S. Wei, Y. Li, *Angew. Chem.*, 2016, **55**, 10800-10805.
- 52 K. N. Kudin, B. Ozbas, H. C. Schniepp, R. K. Prud'homme, I. A. Aksay, R. Car, *Nano Lett.*, 2008, **8**, 36-41.
- 53 G. Zhang, W. Lu, F. Cao, Z. Xiao, X. Zheng, *J. Power Sources*, 2016, 114-125.
- 54 F. Pan, J. Jin, X. Fu, Q. Liu, J. Zhang, *ACS Appl. Mater. Interfaces*, 2013, **5**, 11108-11114.
- 55 Y.Z. Chen, C. Wang, Z.Y. Wu, Y. Xiong, Q. Xu, S.H. Yu, H.L. Jiang, *Adv. Mater.*, 2015, **27**, 5010-5016.
- 56 Z. Zhang, M. Dou, H. Liu, L. Dai, F. Wang, *Small*, 2016, **12**, 4193-4199.
- 57 H. Zhang, S. Hwang, M. Wang, Z. Feng, S. Karakalos, L. Luo, Z. Qiao, X. Xie, C. Wang, D. Su, Y. Shao, G. Wu, *J. Am. Chem. Soc.*, 2017, **139**, 14143-14149.

View Article Online
DOI: 10.1039/C8TA00439K

TOC



A facile strategy for tuning the dimensions and structures of nitrogen-doped carbon nanomaterials as ORR catalysts has been demonstrated.